

Laser induced nanoparticle formation

P. Heszler^{a,*} and L. Landström^b

^a The Ångström Laboratory, Institute of Materials Science, Department of Solid State Physics, Uppsala University, Box 534, SE-751 21 Uppsala, Sweden

^b The Ångström Laboratory, Department of Materials Chemistry, Uppsala University, Box 538, SE-751 21 Uppsala, Sweden

ABSTRACT

General aspects, such as control of size-distribution, agglomeration/coagulation and material properties are discussed for laser-based generation of nanoparticles. Two model systems are presented, i) laser-assisted chemical vapor deposition (LCVD) of tungsten nanoparticles by H₂ reduction of the excited tungsten fluoride precursor gas (WF₆) and ii) laser ablation (LA) of tungsten and carbon targets at atmospheric pressure for W and C nanoparticle formation.

Size-distributions of the nanoparticles are determined by electron microscopy (TEM) for the LCVD depositions and in-situ by a differential mobility analyzer and a particle counter for the LA experiments. The tungsten deposition rate is measured by X-ray fluorescence spectroscopy; materials characterization is performed by electron and X-ray diffraction techniques, Raman spectroscopy and X-ray photoelectron spectroscopy.

The agglomeration/coagulation for LCVD is followed i) by the size-distribution measurements and ii) by optical emission spectroscopy of the emitted thermal (black-body) radiation of the laser-heated nanoparticles. Additionally, optical spectroscopy of the thermal radiation allows determining the temperature of the laser-heated nanoparticles.

During laser ablation the size distributions and the amount of desorbed/ablated material are monitored for different ArF excimer laser parameters (fluence, rep. rate).

The main and most important aspects of the presented techniques are compared and discussed.

Keywords: nanoparticles, laser assisted CVD; laser ablation, size-distribution, tungsten, differential mobility analyzer

1. INTRODUCTION

Shortly after their discovery, lasers became widely used for materials processing¹. Laser radiation can be applied for surface modification (both morphological and chemical), for material deposition (e.g. laser-assisted chemical vapor deposition (LCVD)), or for material removal, most frequently called laser ablation (LA). This latter sometimes is referred as dry etching. If the laser ablated material is used for thin film deposition, then the technique is called pulsed laser deposition, PLD. The advantage of using laser sources, in general, stems from the possibility to control the energy deposition into a system in time (if pulsed lasers are used) and/or space. Herby, the material processing can be significantly directed/tailored as desired.

Nanoparticles (NP) are interesting in nature for their small size (max. 100 nm). Furthermore, the properties of the particles depend on their size, especially in the “real” nm region (about and below 10 nm). Crystalline NPs are frequently referred as nanocrystals (NC), while the materials constructed by NPs and/or NCs often called nanostructured materials (NsM). All of them are subject to intensive research. Due to the mesoscopic properties of the nanoparticles in connection with the increased significance of grain boundaries in NsM, these show different, mostly

* Contact author: Peter.Heszler@Angstrom.uu.se; phone + 46 18 471 7232; fax + 46 18 50 01 31. Also at Research Group of Laser Physics of the Hungarian Academy of Sciences, P.O. Box 406, H-6701 Szeged, Hungary.

superior qualities compared to their bulk counterparts. To name a few examples: high coercive force² and giant magnetoresistance for magnetic NsM³, high flow stress in connection with very high thermal stability, super plasticity and hardness increase, see review papers^{4,5}.

Nanoparticles and nanoparticle films can be fabricated by different methods such as sol-gel, mechanical (milling) and gas phase methods. The gas phase techniques have the advantage, especially the evaporation methods, that ultra-clean particles and films can be deposited⁶. Using this latter technique, the nanoparticles are formed through condensation from an oversaturated vapor.

However, for materials with high melting temperature the evaporation methods possesses difficulties. To produce particles from these kinds of materials, other techniques are required to put the precursor element(s) into the gas phase. Such methods can be laser ablation and chemical vapor decomposition or deposition (CVD). By using LA, a material is evaporated by focusing the pulsed, high power laser beam onto a solid target in an ambient atmosphere and then the particles are condensed from the ablation plume. Applying CVD, the gas phase precursor compounds decompose or react to form solid particles. These CVD processes are often assisted by lasers (LCVD) as it was already mentioned. The advantages of the laser activation in CVD processes are i) increased deposition rate and/or ii) decreased processing temperature, iii) optical emission spectroscopy can be used for process monitoring in many cases and iv) the degree of oversaturation can be easily reached for particle condensation.

In typical PLD experiments the ambient pressure is low (< 0.1 mbar or less) and the laser-evaporated material from the target is condensed onto a substrate, usually yielding high quality films⁷. However, at elevated pressures (> 10 mbar) nanoparticles can be condensed from the laser-evaporated material. For both thin film and nanoparticle deposition the advantage of PLD stems from its versatile vaporization capability resulting in that a wide variety of nanoparticle materials can be produced at low temperature, e.g., Si^{8,9}, different metals as Cu and Ag¹⁰, ceramics Co₃O₄¹¹, other oxide composites^{12,13}, and nitrides, e.g., AlN¹⁴. The size-distribution of the particles is an important issue if application is concerned as well as understanding the processes leading to the particle formation. However, there are only a few measurements on in-situ determination of the size-distribution of the generated particles during the ablation process^{15,16}.

Several kinds of nanoparticles have been generated by LCVD such as Si, Si₃N₄ and SiC by CO₂ laser driven pyrolysis already in the 60s-70s¹⁷. TiC¹⁸, Fe and iron-carbides¹⁹, carbon²⁰, MoS₂²¹, CN_x²², Al₂O₃²³, nanocomposite ternary Si-C-N powders²⁴ were also prepared by CO₂ laser driven pyrolysis. Photolytic (UV excitation) LCVD is also capable of generating ultrafine powders such as nanoparticles containing both iron and carbon²⁵ and tungsten nanoparticles²⁶. An interesting characteristic of nanoparticle generation by LCVD is that the interaction of laser light and particles results in detectable blackbody-like radiation of the hot particles²⁷.

The aim of this work is to present results on nanoparticle formation by LA and LCVD and to compare the most important characteristics of the generated particles such as size-distribution, structure and chemical composition. For the size-distribution measurements of LA we applied the Differential Mobility Analyzing (DMA) technique, originally developed for aerosols²⁸, allowing in-situ measurements.

2. NANOPARTICLE GENERATION, EXPERIMENTAL

2.1 Laser ablation

To determine the size distribution of nanoparticles generated by LA, we applied the experimental arrangement depicted in Figure 1. As target material we choose tungsten and carbon since these are high melting point materials and cannot be prepared by simple evaporation techniques. The nanoparticles were generated by excimer laser (193 nm) ablation of tungsten and carbon targets in N₂ and Ar atmosphere at 1 bar pressure in a flow-through arrangement with a flow-rate of 1 l/min. The target was rotated and a circular diaphragm, illuminated by the laser beam, was imaged onto the surface of the targets by a 10 cm focal length spherical lens. Laser fluence, ablated spot size and repetition rate were varied from 0.2 to 8 J/cm², 50 to 420 μm in diameter and 2-50 Hz, respectively. A radioactive ⁸⁵Kr neutralizer charged the generated particles and their size-spectrum was determined by a differential mobility analyzer (DMA) and a condensation particle counter (CPC) system. The DMA classifies the charged particles on the base of their electrical

mobility (depending on the diameter) in presence of a sheath gas flow²⁸. The size-window of the nano-DMA (TSI Incorporated) was 7 – 133 nm at the applied sheath flow rate (4 liter/min). Deposition of the particles took place, after the DMA, through a 0.5 mm (diameter) nozzle in an electrostatic precipitator.

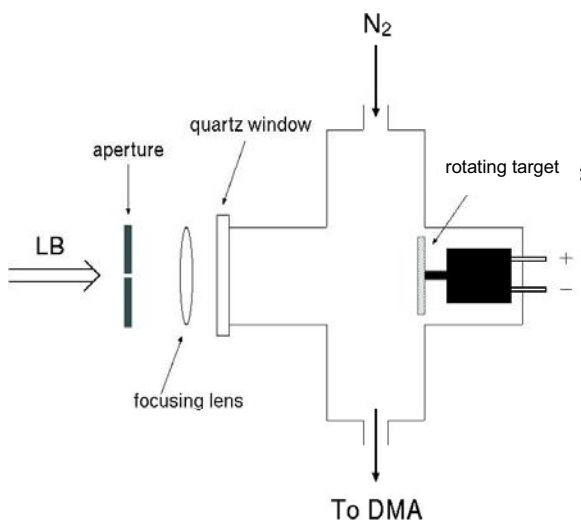


Figure 1. Schematic view of the experimental arrangement for nanoparticle generation by laser ablation. LB and DMA denote laser beam and differential mobility analyzer, respectively.

2.2 Laser assisted chemical vapor deposition

The experimental set-up for tungsten nanoparticle generation by LCVD consisted of a stainless steel vacuum chamber with cross section of 12 cm². The reactor was used in a flow-through arrangement, with a quartz window at the front to deliver the laser beam into the reactor. Argon gas purge was applied to avoid deposition/condensation on the front window. A vertical tube-connection of the chamber was designed, ending by a quartz window to allow optical spectroscopic observations during the experiments, see Figure 2.

For tungsten nanoparticle formation a gas composition of WF₆/H₂/Ar was used at different molar ratios at 20 mbar and 32 sccm total flow. The position of deposition and optical observation was 9 cm downstream relative to the WF₆ entrance.

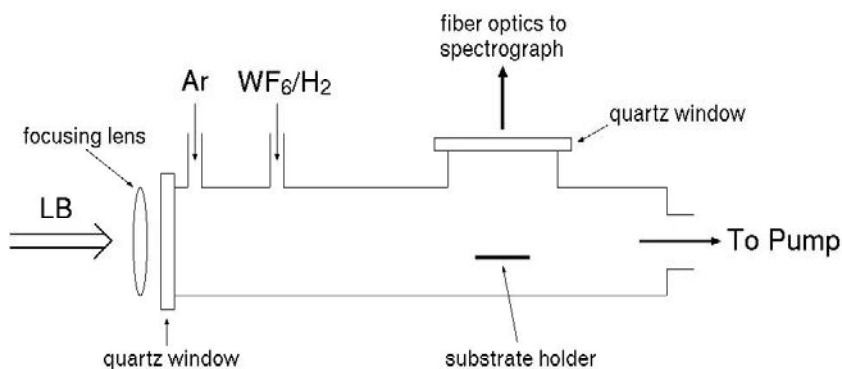


Figure 2. Experimental arrangement for laser-assisted deposition of tungsten nanoparticles. LB stands for laser beam.

A Lambda Physik ArF excimer laser ($\lambda = 193$ nm) was used with a pulse width of 15 ns (FWHM) and a repetition rate of 50 Hz for the photolysis of the CVD reactants. The beam was aligned in parallel to the stainless steel tube and

slightly focused by a cylindrical quartz lens with a focal length of 38 cm. The fluence (at the position of deposition) was typically between 80 and 160 mJ/cm².

An optical detection system consisting of a Czerny-Turner type grating spectrograph, a Charge Coupled Device (CCD) detector and an Optical Multichannel Analyzer (OMA III of EG&G) was used for the optical inspection of the process. A 150/mm grating allowed 1.8 nm spectral resolution and ± 0.2 nm wavelength accuracy. The CCD detector was gated in the 100 ns - 1 μ s range and overall exposure time of 1 s was used during the optical emission spectroscopic (OES) measurements. Delay between the laser and gate pulse was varied from 100 ns to 12 μ s. A tungsten-strip calibration lamp was used to determine the relative transfer function of the optical detection system. For the temperature determination of the nanoparticles due to laser heating, the recorded and corrected spectra were fit by the corresponding Planck curve²⁷. The intensity of the thermal radiation was obtained by integrating the spectrum of the emitted radiation over the monitored wavelength-window (400-700 nm).

The generated nanoparticles, for the two methods mentioned above, were examined by transmission and scanning electron microscopy (TEM, SEM), X-ray diffraction (XRD), X-ray photoelectron spectroscopy (XPS), Raman spectroscopy and energy disperse X-ray spectroscopy (EDS). The tungsten deposition rate of the LCVD was measured by X-ray fluorescence spectroscopy (XRF).

3. RESULTS AND DISCUSSION

3.1 W nanoparticles by laser ablation

SEM pictures of DMA size-selected and deposited particles (40 nm in diameter), generated by tungsten ablation in N₂ atmosphere, can be seen in Figure 3. For short deposition times the particles were found to be separated and one can see monodispersity in size. For longer deposition times a high degree of agglomeration of the deposited particles was observed.

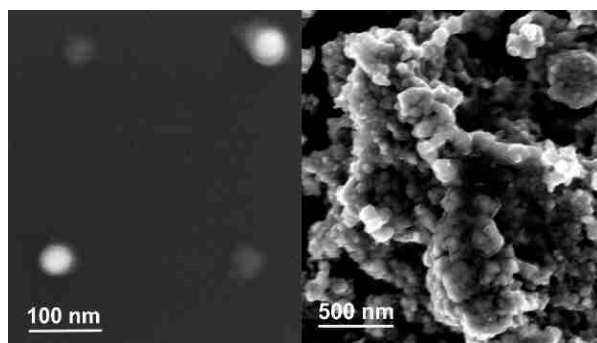


Figure 3. SEM micrographs from size-selected (40 nm in diameter) particles produced at ~ 8 J/cm² laser fluence at different deposition times. Left 5 minutes and right 45 minutes, respectively.

XPS analysis was performed on polydisperse particles (no size-selection was made). From the W 4f region of the spectrum (Figure 4a) one can observe the W-W bonding from the 4f_{7/2} and 4f_{5/2} peaks at 31.0 and 33.2 eV, respectively. The relative intensities between the f peaks and the shoulders at higher binding energies suggest that tungsten bonds to a more electronegative element (nitrogen and oxygen in this case). Nitrogen and W-N bonding was also confirmed by the shift of the N 1s peak towards lower binding energy (~ 397.3 eV, Figure 4b). Taking the sensitivity factors in consideration, and relative intensities from the W 4f and N 1s peaks resulted in an elemental composition of WN_{0.3}. Small amounts of oxygen were also detected due to rapid oxidation of tungsten as the samples were exposed to laboratory air. Grazing incidence XRD of polydisperse samples (laser fluence 8 J/cm²) revealed an amorphous phase of the particles, i.e., no distinct diffraction pattern have been obtained.

Similar results were found regarding the materials characterization of deposited polydisperse carbon nanoparticles generated by carbon ablation in N_2 ambient. An elemental composition of CN_x ($x \sim 0,1$) could be obtained by XPS analysis, and Raman spectroscopy showed amorphous/turbostratic structure of the particles. However, by replacing the N_2 ambient to Ar, amorphous elemental W and C particles could be formed.

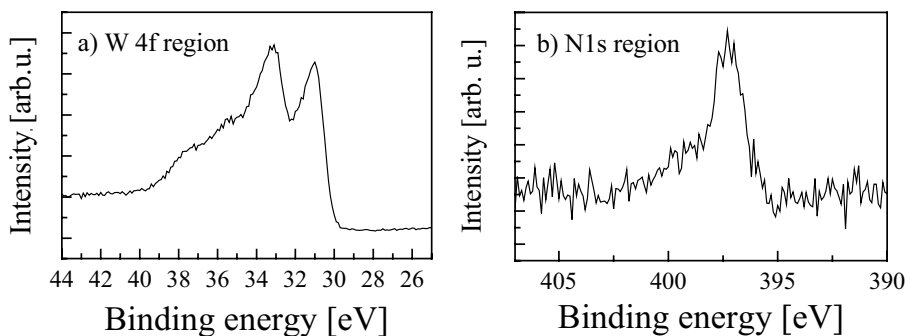


Figure 4. XPS spectra from polydisperse particles generated by ArF excimer laser ablation of W in N_2 atmosphere. a) W 4f and b) N 1s regions, respectively.

Size distribution spectra of $WN_{0.3}$ and CN_x ($x \sim 0,1$) NPs, generated by LA, can be seen in Fig.5 and Fig.6, respectively, while the ablated mass (integrated over the measured size window 7-133 nm) laser fluence dependence is depicted in Fig.7. As the fluence is increased, the increment of ablated mass is small at low fluences, but an abrupt increase can be found at $\sim 6 J/cm^2$ for W and $\sim 1 J/cm^2$ for carbon. Since the ablation threshold (Φ_{th}) is related to significant material removal, it is thus concluded that the multi-shot ablation threshold for tungsten and carbon is $\sim 6 J/cm^2$ and $\sim 1 J/cm^2$ respectively, for the laser source used ($\lambda = 193 nm$). A saturation for the detected mass of carbon NPs can be seen at $\sim 2.5 J/cm^2$ in Fig.7. This can be explained by that larger particles than the higher end of the detection window of the DMA + CPC setup (133 nm) are mostly formed as the laser fluence is further increased above $2.5 J/cm^2$.

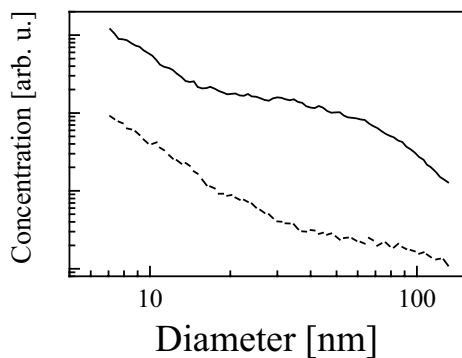


Figure 5. Typical size distribution spectra of $WN_{0.3}$ nanoparticles obtained by LA of tungsten in N_2 ambient at two different laser fluences, with solid and dotted lines corresponding to 8.3 and 4.4 J/cm^2 , respectively. Note the log-log scale.

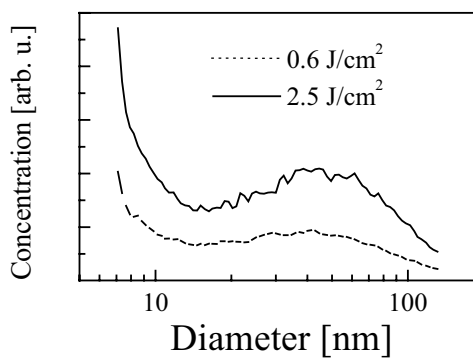


Figure 6. Size distribution spectra of CN_x nanoparticles ($x \sim 0,1$) obtained by laser ablation of graphite in N_2 ambient at two different laser fluences indicated in the figure. Note the log-lin scale.

The NP size distributions, both for C and W, contain mostly small particles ($< 20 nm$ in diameter) below the ablation threshold (see Fig. 5 and 6). This small-sized contribution can be found at all fluences investigated, and it is noted that the shape of this distribution cannot be fitted to a lognormal one. Concentration of larger ($> 20 nm$) particles relative to the smaller ones increases only above Φ_{th} as the fluence is increased. If the shape of the distribution below Φ_{th} is taken as background and subtracted from the high fluence spectra, a distribution (of the particles $> 20 nm$) that resembles a lognormal can be obtained.

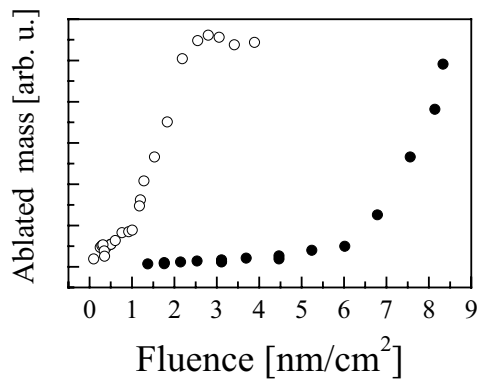


Figure 7. Ablated mass (integrated over the size spectra) versus laser fluence for $WN_{0.3}$ (solid points) and CN_x nanoparticles ($x \sim 0,1$ open circles). The laser repetition rate was 2 Hz, spot diameters were 210 and 500 μm for W and C ablation, respectively.

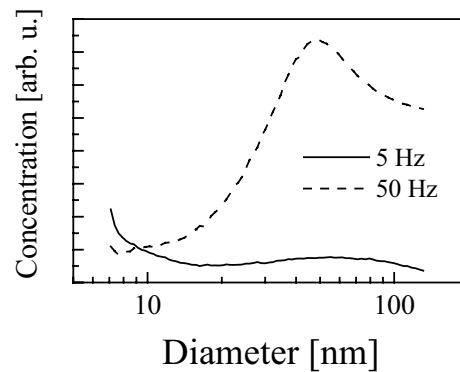


Figure 8. Size distribution spectra of CN_x nanoparticles ($x \sim 0,1$) for different laser repetition rates indicated in the figure. Laser fluence 1.9 J/cm^2 .

The ablation process can be divided in two different parts, the low yield desorptive and the high yield (stoichiometric) forward peaked component, respectively. These two parts are simultaneously present above Φ_{th} , however only the desorptive component can be found below Φ_{th} (see Figures 5 and 6). This latter has a more sensitive angular dependence compared to the forward directed part⁷. Based on the facts that i) appearance of the broad "peak" for larger particle-sizes takes place above Φ_{th} , ii) the small-sized contribution is present at all investigated fluences; we conclude the following. The nanoparticles yielding the dominantly small sized (< 20 nm in diameter) spectra are condensed from the desorptive part and the larger diameter NPs above Φ_{th} are condensed from the forward directed, "real" ablation. This latter can be described as a thermal process, however precise modeling of the ablated process shows that the desorptive part is a photochemical (i.e. non-thermal) process.²⁹

At higher (above ~ 30 Hz) laser repetition rate the concentration of small nanoparticles decreases relative to the larger ones for particles generated by carbon ablation, see Fig.8, but this effect could not be seen for tungsten (figure not shown). Considering the flow rate of the background N_2 gas and the volume of the ablation plume, it can be concluded that the laser pulses interact with the particles produced by the previous shots at laser repetition rates above ~ 10 Hz. This results in elevated temperatures of the nanoparticles (see sect. 3.2.3). Evaporation rates of 10 nm (in diameter) C and W nanoparticles were calculated based on Klots' model.³⁰ The calculated values show, also considering the temperature decreasing rate of the particles³¹, that significant size change for C can take place. In addition, carbon has significantly higher evaporation rate, ~ 30 times more than tungsten at e.g. 3600 K. Further considering that the 10 nm C and W particles' heat capacity ratio is 1.16 and the absorption cross section of carbon is ~ 3 times higher at $\lambda = 193$ nm than that of tungsten (calculated on the basis of Mie theory), it follows that the total number of evaporated atoms at elevated temperatures is definitely higher for carbon than for tungsten. This explains the fact that the concentration of particles under 20 nm in diameter decreases with increasing repetition rate for carbon but not for tungsten. We note that although the calculations were made for pure C and W particles, the observed N content of the generated nanoparticles does not change our qualitative results.

Concerning practical consequences, it can be seen that high concentrations of smaller nanoparticles (< 20 nm in diameter) are formed below the ablation threshold during LA of tungsten and carbon at atmospheric pressure. In nanotechnology, it is usually these small particles that are desirable. Thus, to increase their yield, a fluence somewhat below Φ_{th} , large spot-size and high repetition rate is to be preferred. However, for carbon the high repetition rate has to be accompanied with a high flow rate of the ambient gas, otherwise the produced particles can be evaporated by subsequent laser pulses (see Fig.8).

3.2. W nanoparticles by photolytic LCVD

Tungsten nanoparticles, generated by UV laser-assisted chemical vapor deposition of $WF_6/H_2/Ar$ gas mixture, can be seen in Fig. 9a, while a corresponding electron diffraction pattern is shown in Fig. 9b.

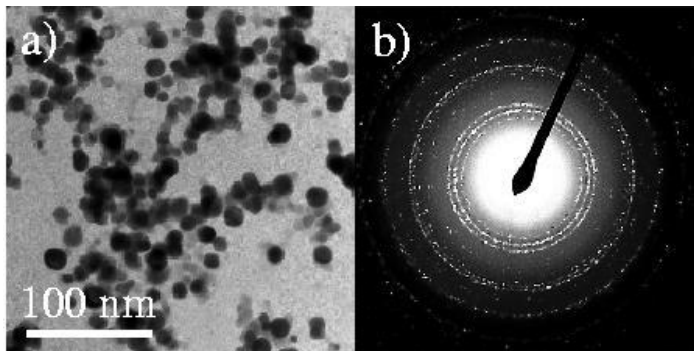


Figure 9. a) TEM image and b) electron diffraction pattern of LCVD deposited tungsten particles. Laser fluence 120 mJ/cm^2 , 165 Pa H_2 and 115 Pa WF_6 partial pressures, total pressure 20 mbar .

The ring pattern corresponds well to β -W, a metastable phase that is assumed to be stabilized by impurities (e.g., fluorine³² or oxygen³³). Traces of F and O contamination were found by Energy Disperse X-ray Spectroscopy, confirming the impurity stabilization. X-ray diffraction pattern (not shown) of the deposits also corresponded to β -W.

In the following we present results regarding how the size distribution and deposition rate of the particles depends on the partial pressure of the reactants in the $WF_6/H_2/Ar$ gas mixture.

3.2.1 H_2 partial pressure dependence

Size-distribution histograms for five different H_2 partial pressures (p_{H_2}) are shown in Fig. 10. It can be seen that the dominant size is $\sim 12 \text{ nm}$ in diameter for all examined partial pressures and only a slight increase in mean diameter of the particles is observed, see also Fig. 11.b.

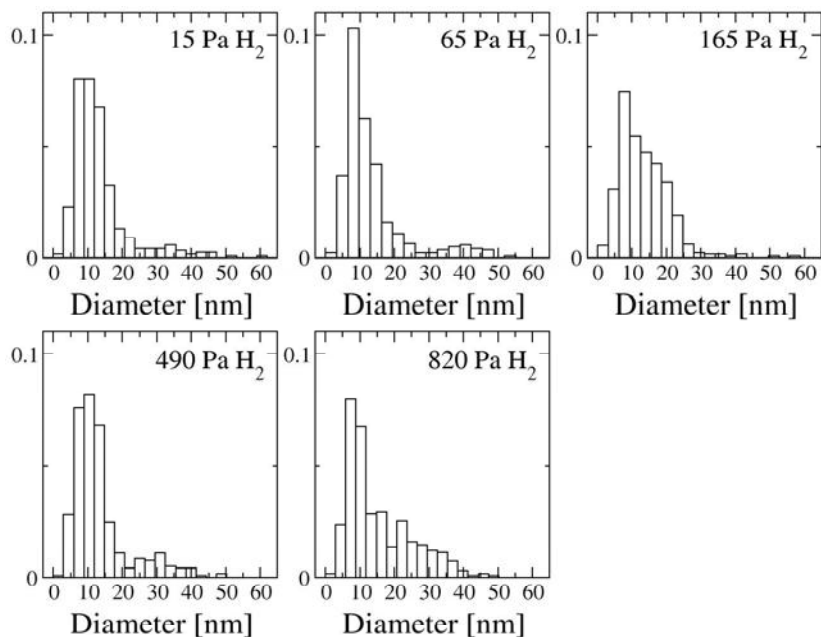


Figure 10. Normalized size-distribution histograms for five different H_2 partial pressures. Diameters of 400 particles were measured for each p_{H_2} from TEM BF micrographs. WF_6 partial pressure 30 Pa with a total pressure of 2000 Pa .

The tungsten deposition rate dependence on p_{H_2} is shown in Figure 11a. A steep increase of the XRF signal (that is assumed to be proportional to the deposition rate) can be observed up to ~ 60 Pa, where the deposition rate reached a saturation level and stayed approximately constant up to 500 Pa. Above this value a slight increase of the deposition rate was observed. No tungsten can be deposited at zero H_2 partial pressure, which can be explained by the chemistry of the net reaction for tungsten formation:



where (g) and (s) denote gas or solid phase, respectively. We note that in principle, the laser photons could strip away the F atoms from the WF_6 molecules, giving rise to the formation of W atom vapor and thereby clusters or nanoparticles. However, this reaction sequence is very unlikely due to the non-linearly coupled photolytic reaction steps (one laser photon at 193 nm can strip away only one F atom from the WF_6 and the subfluorides). The tungsten deposition rate increases rapidly with p_{H_2} in the 10-50 Pa p_{H_2} interval, understood as access of H_2 within the reaction-zone is in deficit with respect to the 30 Pa WF_6 partial pressure - in analogy with reaction (1). The maximum deposition rate is observed at ~ 60 Pa H_2 , however in accordance with the stoichiometry of the reaction described by eq.(1) and the applied partial pressure of WF_6 (30 Pa), this should be found at 90 Pa H_2 partial pressure. This discrepancy is explained by the change in stoichiometry of the net reaction due to the photolytic contribution during LCVD, i.e. less H_2 is needed for the tungsten formation since the laser photons strip away fluorine atoms.

There is no significant change in the measured size-distributions as the p_{H_2} is varied (see Fig. 10). This is not surprising considering the fact that the excess H_2 does not yield higher tungsten particle concentration, if the H_2/WF_6 partial pressure ratio exceeds the photolytic stoichiometry (~ 2). The slight increase of the deposition rate and mean size at high p_{H_2} (Fig.11) is most likely due to thermal CVD according to eq.(1) on the surface of the hot particles. The observed size distributions deviate from the lognormal type that is explained by agglomeration and further coalescence of the particles occur at ~ 30 Pa p_{WF_6} . This assumption is verified in the following subsection.

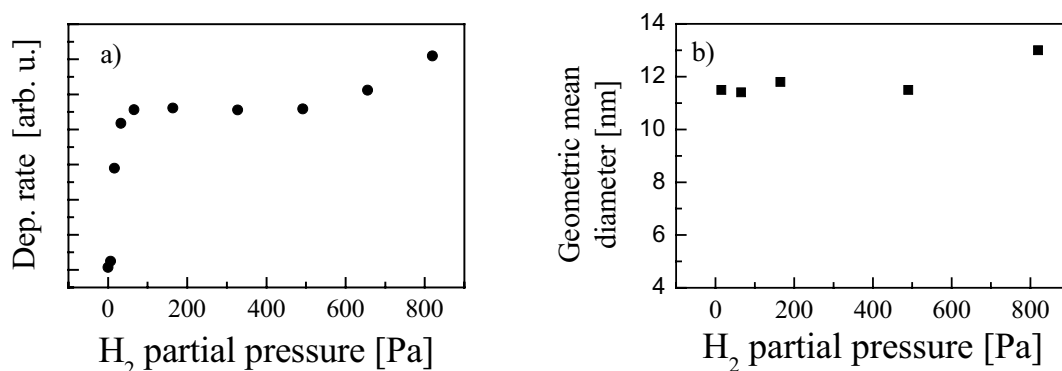


Figure 11. a) Tungsten deposition rate and b) geometric mean diameter of W nanoparticles as a function of H_2 partial pressure, respectively. The deposition rate was measured by XRF, the mean diameter was determined by TEM measurements, see the histograms in Fig.10.

3.2.2 WF_6 partial pressure dependence

It can be naturally expected that the most significant effect on the size distribution of the LCVD generated W nanoparticles the W precursor concentration has. (Although it is noted that without H_2 reactant no particles are formed.) This can be seen in Fig.12 left panel, where the size distributions of the generated W particles for different WF_6 partial pressures (p_{WF_6}) are shown. Only at the lowest p_{WF_6} (15 Pa), does the distribution follow the lognormal type. At higher p_{WF_6} (> 30 Pa) the deviation (from a lognormal distribution) becomes more significant, and it can be seen that the mean size of the particles increases and the distributions are broadened.

If the particles are formed during an equilibrium condensation from an oversaturated vapor - with constant oversaturation ratio - the expected result is a lognormal size distribution of the particles³⁴. Below the so called coagulation limit (the concentration value where significant coalescence takes place), the Residence Time Approach (RTA) model can be applied to explain the resulting lognormal distribution³⁵. In the RTA model the particle growth is assumed to be governed purely by vapor condensation and no aggregation or coagulation of the particles occur. It has been shown that for vapor condensation the particle volume is proportional to the residence time (the average time that the particles stay in the growing zone) and that has a lognormal distribution. Consequently, the particle radius also has a lognormal distribution. This model explains the obtained lognormal size distribution at low partial pressures of WF_6 (Fig.12 left). However, the broadening and deviation (from a log-normal type) of the size distributions above ~ 30 Pa partial pressure indicates that agglomeration/coagulation of the particles occur supported by TEM records, see Fig. 12 right panel. It has to be noted that a lognormal distribution can also be preserved above the coagulation limit - if the total mass is conserved and a sufficient number of collisions takes place - due to self-preserving behavior of the coagulation process and the initial distribution³⁶. However, an open system was used in our studies, therefore the total mass of the agglomerated particles was not conserved. The residence time in the reaction-zone was small, a few seconds, i.e. sufficient number of collisions couldn't take place. In addition, only partial coalescence of the particles occurred in the aggregates. These facts explain the distorted distributions (relative to lognormal and shifted towards larger diameters) for high partial pressures of WF_6 (> 30 Pa).

The mean size of the particles increases with the precursor concentration see Fig. 13b. More precisely, the geometric mean volume of the particles increases linearly with the WF_6 partial pressure. We cannot account for this observation at the present stage of the investigations, ongoing research is in progress. It seems that a significant growth of the particles can be attributed to partial coalescence of the particles in the agglomerates.

As a practical consequence it can be stated that in order to obtain a narrow size distribution of the particles one has to avoid agglomeration/coagulation and for that a low WF_6 partial pressure is needed. On the other hand it is worth noting that if higher p_{WF_6} is used, the aggregation/coagulation of particles can also be avoided by decreasing the residence time of the particles in the reactor.

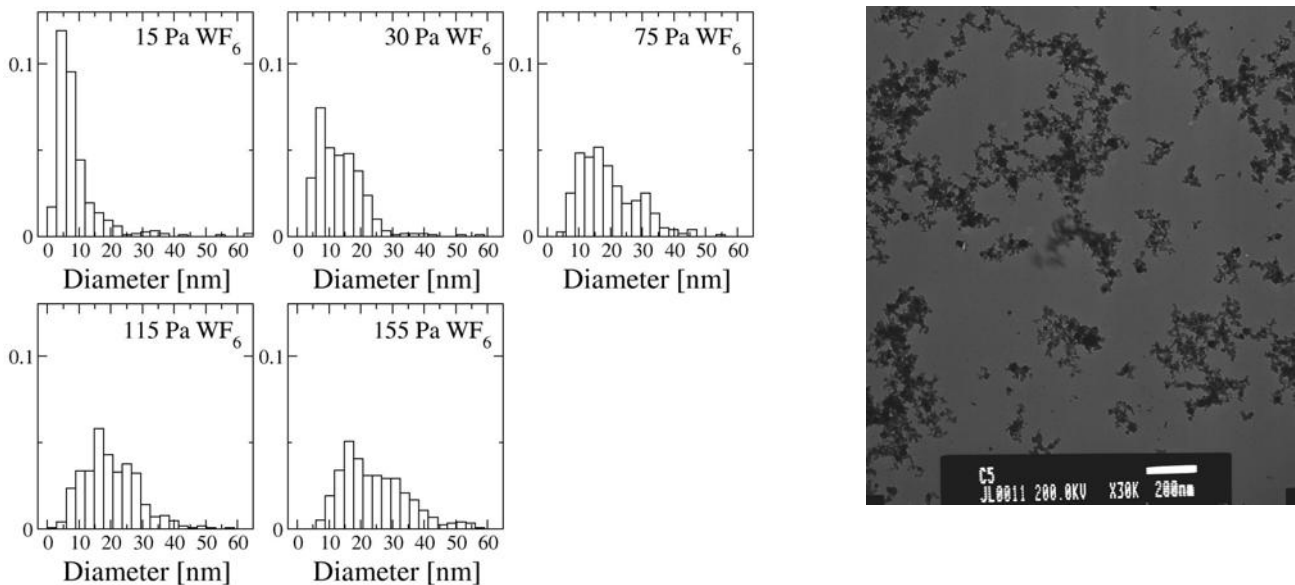


Figure 12. Left: Normalized size-distribution histograms for five different WF_6 partial pressures. Diameters of 400 particles were measured for each p_{WF_6} from TEM BF micrographs. Right: TEM picture of agglomerated particles at 115 Pa WF_6 partial pressure. H_2 partial pressure 165 Pa with a total pressure of 20 mbar.

The rate of deposition of tungsten increases continuously as p_{WF_6} is elevated, slightly deviating from a linear behavior at partial pressures above ~ 80 Pa, see Fig.13a. Earlier studies showed a linear dependence³⁷ and the slight deviation in Fig.13a can be explained by that the $H_2:WF_6$ ratio is less than 2 above 80 Pa, i.e. less than the necessary ratio for maximum amount of tungsten formation taking into account the photolytic contribution, see the previous section.

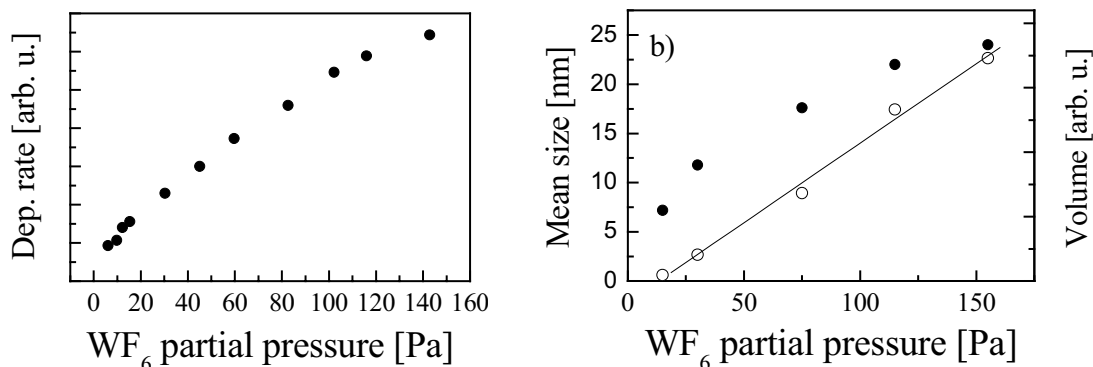


Figure 13. a) Rate of deposition of tungsten from XRF measurements, and b) mean size (diameter, solid points from Fig. 12), dependence on WF_6 partial pressure. The open circles denote the mean volume of the particles derived from the mean size. H_2 partial pressure 165 Pa at a total pressure of 20 mbar. The solid line in Fig. b represents the best linear fit.

3.2.3 Optical emission studies

Corrected emission spectra at different delay times with respect to the short laser pulse (15 ns) and the corresponding fitted Planck curves are shown in Fig. 14a.

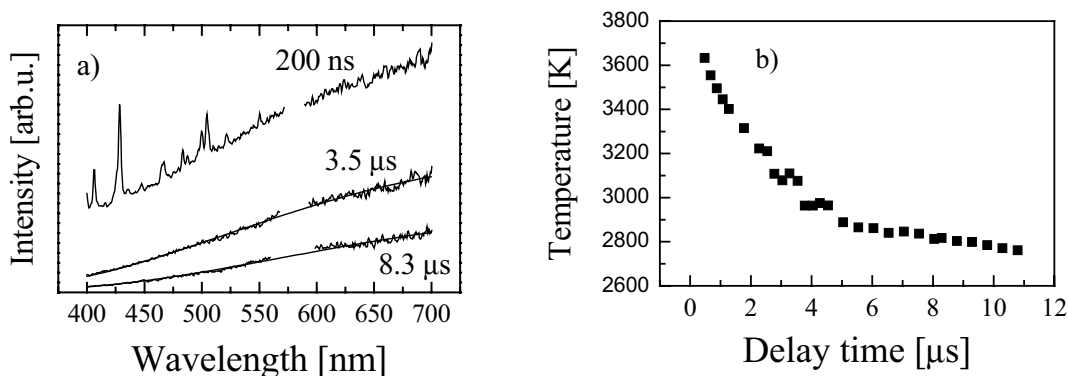


Figure 14. a) Measured and corrected emission spectra of tungsten nanoparticles at different delay times with respect to the laser pulse. The solid lines represent the best Planck curve fits for temperature determination of the laser-heated particles and b) temperature versus delay time. WF_6 partial pressure 20 Pa, total pressure 20 mbar, laser fluence 115 mJ/cm^2 . Tungsten nanoparticle mean size 10 nm. The discontinuity at ~ 580 nm in the spectra in Fig.14a is due the cut of the 3rd order of scattered 193 nm laser line.

The good agreement between the measured and fitted broad-band spectra indicates that the laser heated nanoparticles emit thermal radiation with corresponding high temperatures. It could also be observed that spectral lines were superimposed on the thermal radiation at early delays (see Fig.14a at 200 ns delay) and these lines were identified as atomic tungsten emission lines.

The temperature versus delay time is depicted in Fig.14b. It can be seen that the derived initial temperature (at $0.5 \mu\text{s}$ delay, when no elemental lines interfered with the fitting-procedure) was ~ 3650 K that is close to the melting point of

tungsten (3695 K). This value at 0.5 μs combined with the temperature-decreasing rate at the earliest delays ($\sim 300 \text{ K}/\mu\text{s}$), shows that the particles are - at least partially - melted (at a laser fluence of $115 \text{ mJ}/\text{cm}^2$ in this case) during - and a short time after - the laser pulse. Plot of the temperature decrease shows an initially fast (slightly declining) rate of decrease (for delays $< 4 \mu\text{s}$) and a slower rate of decrease at longer delays ($> 4 \mu\text{s}$), see Fig. 14b.

As it is known, free hot particles or clusters of atoms cool down by three different mechanisms. These are: i) evaporation of atoms/molecules (unimolecular decay), ii) thermionic electron emission and iii) thermal (blackbody-like) radiation. In addition, when the particles are surrounded by a gas, inelastic collisions between the particles and the ambient gas species also result in energy-transfer from the particles. A detailed analysis of the measured data depicted in Fig. 14b showed that evaporation of atoms is the dominant cooling mechanism at elevated temperatures ($> 3000 \text{ K}$), the temperature decreasing rate (dT/dt) is high, $\sim 300 \text{ K}/\mu\text{s}$ in the first μs . A combination of radiative cooling (with $dT/dt \sim 5 \text{ K}/\mu\text{s}$) and heat transfer by inelastic collisions (with $dT/dt \sim 20 \text{ K}/\mu\text{s}$) are dominant at temperatures below $\sim 3000 \text{ K}$ for a $\sim 10 \text{ nm}$ in diameter W particle. Thermionic emission is negligible due to charging. The evaporation at high temperatures is also confirmed by the fact that elemental W lines were superimposed on the spectra of the thermal radiation at early delays. This can be explained by evaporation of electronically excited tungsten atoms from the hot particles, and de-excitation of these atoms results in the observed W atomic lines (see spectrum in Fig. 14b at 200 ns delay). In addition, the strong evaporation can yield a slight size decrease of the particles at elevated laser fluences, see Table 1.

Table 1. Dependence of geometric mean diameter (d_g) on laser fluence (Φ), at 20 mbar total pressure.

Φ [mJ/cm^2]	45	65	90	115	135
d_g [nm]	8	9	9	10	9

The temperature and the intensity of thermal emission of the W nanoparticles as a function of the WF_6 partial pressure (p_{WF_6}) are depicted in Figures 15 a and b, respectively. The nanoparticle temperature decreases approximately linearly ($\sim -1.5 \text{ K}/\text{Pa}$) until $\sim 120 \text{ Pa}$ partial pressure of WF_6 , after which the temperature drops rapidly ($\sim -10 \text{ K}/\text{Pa}$) with increasing p_{WF_6} . The intensity of thermal emission of the NPs increases up to $\sim 30 \text{ Pa}$ p_{WF_6} . With further increasing of p_{WF_6} the intensity goes through first a local minimum at $\sim 75 \text{ Pa}$ then a local maximum at $\sim 110 \text{ Pa}$ and finally drops again.

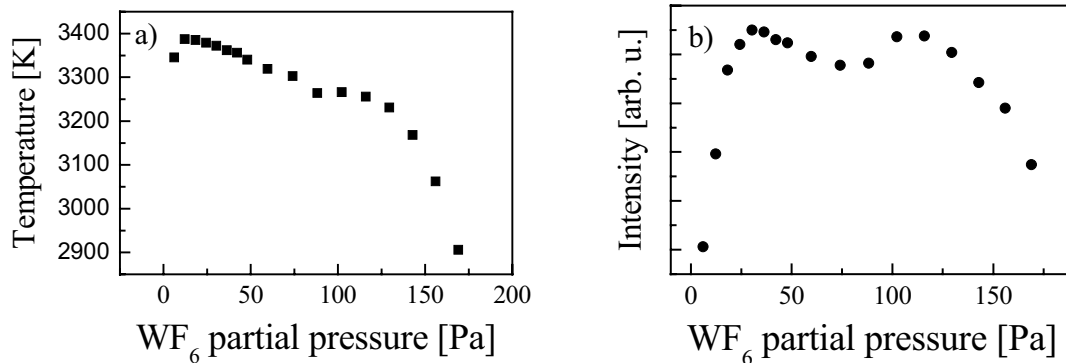


Figure 15. a) Temperature and b) intensity of the blackbody radiation as a function of WF_6 partial pressure. Gate pulse $1 \mu\text{s}$, delay time 500 ns , H_2 partial pressure 165 Pa with a total pressure of 2000 Pa . Laser fluence $120 \text{ mJ}/\text{cm}^2$ and repetition rate 50 Hz .

The temperature decrease of the W nanoparticles with increasing p_{WF_6} can be understood by considering that the elevated WF_6 partial pressure increases the heat conductivity of the ambient gas. The steeper decrease at $\sim 120 \text{ Pa}$ WF_6 is attributed to the significant attenuation of the incident laser beam due to the high concentration of WF_6 and the generated W nanoparticles.

It is known that the absorption cross-section of small particles with radius r , according to the Mie theory, is proportional to r^3 , i.e. the volume of the particles³⁸. Since the heat capacity is also proportional to the volume, thus the initial temperature (after the laser pulse) of the nanoparticles is independent of the size. The temperature decreasing rate, on the other hand, depends on size, but this (not strong) dependence is not taken into account here. Therefore T is considered to be constant for the 1 μs optical gate pulse starting at 0,5 μs delay with respect to laser pulse, as examining the effect of p_{WF_6} . The intensity of the emitted thermal radiation can be written as

$$I(r) = V_o T^4 \int_0^{\infty} n_c(r) A_s(r) \varepsilon(r) dr \quad (2)$$

where V_o is the observed volume (constant), n_c , A_s and ε are the concentration, surface area and emissivity of the nanoparticles, respectively. Since $A_s \sim r^2$ and $\varepsilon \sim r$ (ref³⁸) the emitted intensity is proportional to the total volume of the nanoparticles according to eq.(2). Thus, the rising part of the emitted intensity in Fig. 15b at low p_{WF_6} can be explained by the increasing volume (mass) of the generated nanoparticles in accordance with the result depicted in Fig. 13a. However, further increase of p_{WF_6} results in a drop of the emitted intensity at ~ 30 Pa p_{WF_6} . To account for this effect it has to be noted that eq.(2) is valid only if the particles emit light independently from each other. If the emission comes from agglomerated particles, i) interference, ii) multiple scattering and iii) attenuation should be taken into account. (Points ii) and iii) can be significant only for larger agglomerates.) Therefore it can be assumed that the local maximum at ~ 30 Pa p_{WF_6} can be assigned to the formation of agglomerates of the nanoparticles. Indeed, the narrow and lognormal size distribution at low p_{WF_6} (15 Pa) becomes broader and deviates from the lognormal type at and above 30 Pa, see Fig.12 left panel. In addition, large size agglomerates can be seen in Fig. 12 right panel at relatively high p_{WF_6} (115 Pa). These observations indicate that the local maximum at ~ 30 Pa WF_6 partial pressure can be attributed to the formation of agglomerates. Further and detailed investigations of these phenomena, i.e aggregate formation and light emission from aggregates, are in progress in connection with light scattering measurements from aggregated W nanoparticles³⁹. It can also be concluded that optical emission spectroscopy is capable of monitoring the agglomeration process of nanoparticles formed in LCVD processes.

3.4 Comparing the LCVD and LA methods

Some aspects of the laser-assisted CVD and laser ablation for nanoparticle generation are compared in Table 2.

Table 2. Comparison of LCVD and LA methods for nanoparticle generation.

Aspects	Laser-assisted CVD	Laser ablation
type of material	limited to precursors with appropriate absorption cross sections for common laser wavelength	practically any kind of target material*
mean size	nm -100 nm	nm -100 nm
width of size distribution	can be narrow	wide
varying the mean size	wider possibility	limited
yield	proper for thin film deposition	
crystallinity	crystalline	mostly amorphous [†]
purity	contaminations very likely occurs	high [‡]
high melting point materials	yes	yes
composites	yes	yes

* Reactive ablation can also be used. [†] The amorphous phase can be altered by heating up the particles by subsequent laser annealing.

[‡] Assuming high purity starting (target) materials.

The most significant difference between LCVD and LA, concerning nanoparticle generation, is that inherently, LA yields a wide size distribution of the particles (see Figures 5 and 6), while low precursor concentration for LCVD, avoiding agglomeration, results in significantly narrower size distribution (see Fig.12 left panel). LA produces mostly amorphous phase of the particles, though most likely that can be improved (if crystalline material is preferred) by post-annealing using laser sources. LCVD yields crystalline NPs in our studies. In addition, LCVD gives the possibility to vary the mean size easily by changing the precursor concentration (see Fig. 12). The particle size can also be adjusted in LA by altering the ambient pressure¹⁶, though this is not so straightforward as for LCVD. Some contamination is likely to occur for LCVD from the precursor constituents, while for LA the purity of the target material and ambient gas determines the cleanliness of the generated particles. Other advantage of the LA is that it can be used for practically any kind of target material, while LCDV is limited for proper precursor gas. High laser fluence interacting with the nanoparticles can cause strong evaporation of the particles giving the possibility to shape the size distributions for both LCVD and LA, see Fig.8 and Table 1. The yield of the nanoparticles, of course, depends on the experimental parameters. Generally, an average yield (deposition rate) of $\sim 100 \text{ \AA}/\text{min}$ can be achieved by both methods, which sufficient for thin film deposition. The surface area that can be covered also depends on the experimental conditions. Several cm^2 can easily be covered by relatively simple setups for both LCVD and LA.

CONCLUSIONS

Some aspects of nanoparticle generation by laser-assisted chemical vapor deposition (LCVD) and laser ablation (LA) techniques are presented and compared. LCVD generates narrow size distribution (if agglomeration is avoided) while LA yields wide size distribution of the nanoparticles. LCVD is convenient for varying the mean size of the particles by changing the partial pressure of the precursor gas, while an attractive characteristic of LA is that it is capable of producing particles from practically any kind of target material. On the other hand LCVD is limited to appropriate gas phase precursors absorbing in common laser wavelengths. Crystalline particles can be obtained by LCVD and mostly amorphous by LA, however post-annealing by subsequent laser irradiation can yield crystalline phase for this latter case already in the gas phase. The yield (particle deposition rate) is appropriate for thin film depositions for both methods. By optical emission spectroscopy it is possible to monitor the agglomeration process of nanoparticles in LCVD, as those emit blackbody radiation due to the laser heating. High laser fluence may induce strong evaporation of the nanoparticles thereby giving possibility to tailor the shape of the size distributions for both LCVD and LA.

ACKNOWLEDGEMENTS

Financial supports from Swedish Research Council for the Engineering Sciences and Göran Gustafsson stiftelse are greatly acknowledged. P. H. thanks for partial supports from the OTKA foundation with grant numbers T34381 and TS040759.

REFERENCES

1. D. Bäuerle", *Laser Processing and Chemistry*, 3 edition, Springer Verlag, Berlin, 2000.
2. S. Nafis, X.X. Tang, B. Dale, C.M. Sorensen, G.C. Hadjipanayis, K.J. Klabunde, *J. Appl. Phys.* **64**, 5835, 1988.
3. A.E. Berkowitz, J.R. Mitchell, M.J. Carey, A.P. Young, S. Zhang, F.E. Spada, F.T. Parker, A. Hutten, G. Thomas, *Phys. Rev. Lett.* **69**, 3745, 1992.
4. H. Gleiter, *Acta Mater.* **48**, 1, 2000.
5. A.S. Edelstein, J.S. Murday, B.B. Rath, *Progress in Materials Science* **42**, 5, 1997.
6. C. Hayashi, R. Uyeda, A. Tasaki, *Ultra-Fine Particles: Exploratory Science and Technology*, Noyes, Westwood, 1997.
7. D. B. Chrisey, G. K. Hubler, Eds., *Pulsed Laser Deposition of Thin Films* (John Wiley & Sons, New York 1994)
8. T. Yoshida, S. Takeyama, Y. Yamada, K. Mutoh, *Appl. Phys. Lett.* **68**, 1772, 1996.

9. D.B. Geohegan, A.A. Poretzky, G. Duscher, S.J. Pennycook, *Appl. Phys. Lett.* **72**, 2987, 1998.
10. Z. Pászti, Z.E. Horváth, G. Pető, A. Karacs, L. Guzzi, *Solid State Phenomena* **56**, 207, 1997.
11. Q. Li, T. Sasaki, N. Koshizaki, *Appl. Phys. A* **69**, 115, 1999.
12. M. Kato, *Jpn. J. Appl. Phys. Part 1* **15**, 757, 1976.
13. J.C.M. Marijnissen, S. Pratsinis (Eds.), *Synthesis and Measurement of Ultrafine Particles*, Delft University Press, Delft, 1993.
14. G.P. Johnston, R. Muenchausen, D.M. Smith, W. Fahrenholtz, S. Foltyn, *J. Am. Ceram. Soc.* **75**, 3293, 1992.
15. R.L. Whitlock and G.M. Frick, *J. Mater. Res.* **9**, 2868, 1994.
16. R.M. Camata, M. Hirasawa, K. Okuyama, K. Takeuchi, *J. Aerosol Sci.* **31**, 391, 2000.
17. L.S. Haggerty, W.R. Cannon, in J.I. Steinfeld (Ed.), *Laser-Induced Chemical Processes*, Plenum Press, p. 165, 1981.
18. R. Alexandrescu, E. Borsella, S. Botti, M.C. Cesile, S. Martelli, R. Giorgi, S. Turtu, G. Zappa, *J Mater. Sci.* **32**, 5629, 1997.
19. R. Alexandrescu, S. Cojocar, A. Crunteanu, I. Morjan, I. Voicu, L. Diamandescu, F. Vasiliu, F. Huisken and B. Kohn, *J. Phys. IV France* **9**, 537, 1999.
20. N. Herlin, I. Bohn, C. Reynaud, A. Galvez, J.N. Rouzaud, *Astron. and Astrophys.* **330**, 1127, 1998.
21. E. Borsella, S. Botti, M.C. Cesile, S. Martelli, A. Nesterenko, *Mater. Sci. Forum* **278**, 636, 1998.
22. R. Alexandrescu, F. Huisken, G. Pugna, A. Crunteanu, S. Petcu, S. Cojocar, R. Cireasa, I. Morjan, *Appl. Phys. A* **65**, 207, 1997.
23. R. Alexandrescu, E. Borsella, S. Botti, M.P. Cesile, S. Martelli, R. Giorgi, S. Turtu, G. Zappa, *J Mater. Res.* **12**, 774, 1997.
24. E. Borsella, S. Botti, R. Fantoni, R. Alexandrescu, I. Morjan, C. Popescu, T. Dikonimosmakris, R. Giorgi, S. Enzo, *J. Mater. Res.* **7**, 2257, 1992.
25. K. Elihn, F. Otten, M. Boman, P. Heszler, F. E. Kruis, H. Fissan, J. O. Carlsson, *Appl. Phys. A.* **72**, 29, 2001.
26. P. Heszler, J-O. Carlsson and P. Mogyorósi, *J. Vac. Sci. and Technol. A* **11**, 2924, 1993.
27. P. Heszler, L. Landström, M. Lindstam, J. O. Carlsson, *J. Appl. Phys.* **89**, 3967, 2001.
28. W. Winklmayr, G.P. Reischl, A.O. Lindner, A. Berner, *J. Aerosol Sci.* **22**, 289, 1991.
29. L. Landström, Zs. Márton, N. Arnold, H. Högberg, M. Boman and P. Heszler, submitted for publication
30. C. E. Klots: *Z. Phys. D* **20**, 105, 1991
31. P. Heszler, *Appl. Surf. Sci.* **186**, 538, 2002
32. C. C. Tang and D. W. Hess, *Appl. Phys. Lett.* **45**, 633, 1984
33. G. Hägg and N. Schönberg, *Acta Crystallogr.* **7**, 351, 1954
34. H. G. Scheibel, J. Porstendorfer, *J. Aerosol Sci.* **14**, 113, 1983
35. L.B. Kiss, J. Söderlund, G. A. Niklasson, and C. G. Granqvist, *Nanotechnology* **10**, 25, 1999
36. F. S. Lai, S. K. Friedlander, J. Pich, and G. M. Hidy, *J. Colloid Interface Sci.* **39**, 395, 1972
37. H. Matsuhashi and S. Nishikawa and S. Ohno, *Mater. Res. Soc. Symp. Proc.* **129**, 63, 1989
38. C. F. Bohren and D. R. Huffman: *Absorption and Scattering of Light by Small Particles*, John Wiley & Sons, 1983.
39. L. Landström and P. Heszler, to be published.